*Article*

# Photocatalytic Activity of $Cu_2S/WO_3$ and $Cu_2S/SnO_2$ Heterostructures for Indoor Air Treatment

**Alexandru Enesca [1],* and Luminita Isac [2]**

[1] Product Design, Mechatronics and Environmental Department, Transilvania University of Brasov, Eroilor 29 Street, 35000 Brasov, Romania

[2] Renewable Energy Systems and Recycling Research Center, Product Design, Mechatronics and Environmental Department, Transilvania University of Brasov, Eroilor 29 Street, 35000 Brasov, Romania; isac.luminita@unitbv.ro

* Correspondence: aenesca@unitbv.ro; Tel.: +40-73-2712-472

**Abstract:** Volatile organic compounds (VOCs) are commonly found in indoor spaces (e.g., homes or offices) and are often related to various illnesses, some of them with carcinogenic potential. The origins of VOC release in the indoor environment are in office products, building materials, electronics, cleaning products, furniture, and maintenance products. VOC removal can be done based on two types of technologies: adsorption in specific materials and decomposition via oxidative processes. The present article reports the development and photocatalytic activity of two heterostructures ($Cu_2S/WO_3$ and $Cu_2S/SnO_2$) used for indoor air decontamination. The acetaldehyde removal rate is discussed in correlation with the S-scheme mechanisms established between the heterostructure components but also comparatively with the bare catalysts' activity. Acetaldehyde was considered as a VOC reference because it was found by the International Agency for Research on Cancer to be one of the most frequent air toxins with potential carcinogenic effects. The samples contained monoclinic $WO_3$, tetragonal $SnO_2$, and orthorhombic $Cu_2S$ crystalline structures. The $Cu_2S$ crystallite size in the heterostructure varied from 75.9 to 82.4 Å, depending on the metal oxide substrate. The highest photocatalytic efficiency (75.7%) corresponded to $Cu_2S/SnO_2$, with a constant rate of 0.106 s$^{-1}$ (which was three times faster than $WO_3$ or $SnO_2$ and seven and a half times faster than $Cu_2S$).

**Keywords:** photocatalysis; semiconductors; heterostructure; S-scheme mechanism; acetaldehyde; air decontamination

## 1. Introduction

The development of urban areas and industrial activities has significantly decreased indoor and outdoor air quality. Volatile organic compounds (VOC) are commonly found in indoor spaces (home or office) and are often related to various illnesses, some of them with carcinogenic potential [1–3]. The origins of VOC release in the indoor environment are in office products, building materials, electronics, cleaning products, furniture and maintenance products. VOC removal can be done based on two types of technologies: adsorption in specific materials and decomposition via oxidative processes [4–6]. The adsorption technique is able to capture the pollutant molecules into the sorbent media in a stable form because of the formation of chemical or physical bindings. This method is commonly used in office spaces but has as disadvantages the fast sorbent saturation and removal capability [7,8]. Additionally, the increase in air flow rate or temperature will induce VOC desorption and environmental re-contamination. After saturation, the sorbent must be carefully treated and disposed in special containers, considering the contaminant's hazard potential [9,10].

The decomposition processes use oxidation techniques: photocatalysis, ozonation, or plasma-driven oxidation [11–13]. The photocatalytic air decontamination has the advantage of being activated by the light energy reaching the catalyst surface. Consequently, the pro-

cess can be designed to be energy sustainable because of the use of sunlight or low-energy-consuming light sources. In this case, the catalyst must be a material with high receptivity to both UV and vis spectra. The catalysts are represented by a single component, tandems/heterostructures, or composite materials, which can be activated by the photon absorption with energy equal or higher than the band-gap value [14–16]. Single catalysts such as $TiO_2$ [17], $WO_3$ [18], $ZnO$ [19], $SnO_2$ [20], and $CuInS_2$ [21] show important limitations in terms of reduced light absorbance, fast electron-hole recombination, or low chemical stability in the working environment. Composite materials (graphene/$ZnO$, textiles/$TiO_2$, fly ash/semiconductors, etc.) combine both photocatalytic and absorbance processes and usually exhibit high removal efficiencies [22–24]. The main issue is related with the incomplete decomposition of the absorbed pollutant, which has the potential to be released in the environment. Finally, the heterostructures such as $TiO_2$/$CuInS_2$ (CIS) [25], $TiO_2$/$WO_3$ [26], $SnO_2$/$ZnO$ [27], or $ZnO$/$WO_3$ [28] have the advantage of using an extended light spectra, a reduced charge recombination, and the ability to generate a high quantity of oxidative radicals.

Using innovative materials such as cellulose particles [29], graphene-based nanomaterials and zeolite [30] with high VOC adsorbent capacity represents another approach for gas pollutant removal. These types of adsorbents can reduce their capacity when they reach the saturation point or the adsorption equilibrium. The photocatalytic oxidation of VOCs is a difficult process, and the decomposition pathways and efficiencies depend on various reaction conditions. The humidity is a very important factor influencing VOCs' degradation [31]. High concentrations of water vapor in the working environment are beneficial to the photocatalytic oxidation of VOCs because of the increase in hydroxyl radical development, acting as an oxidizing agent on the surfaces of the photocatalytic materials [32]. However, water molecules and VOC molecules can compete for filling the adsorption active sites, which reduce the photocatalytic efficiency [33].

The present article reports the development and photocatalytic activity of two heterostructures ($Cu_2S$/$WO_3$ and $Cu_2S$/$SnO_2$) used for indoor air decontamination. The acetaldehyde removal rate is discussed in correlation with the Z-scheme mechanisms established between the heterostructure components but also comparatively with bare photocatalyst activity. The influence of the crystalline structure, morphology, and surface composition was also investigated. The results indicated that a facile chemical route procedure can be employed to obtain efficient photocatalytic heterostructures able to work in the removal of toxic pollutants.

## 2. Materials and Methods

### 2.1. Heterostructure Development

Three mono-component and two heterostructures were obtained by the sol-gel technique as follows:

(i) $WO_3$ powder was prepared by adding tungsten hexachloride ($WCl_6$, 99.8%, Acros Organics, Geel, Belgium) in a solvent composed of 2-propanol (100%, Sigma Aldrich, Munich, Germany) and ethanol (100%, Sigma Aldrich, Munich, Germany). The above composition was stirred for 140 min until a light yellow solution was formed. The gel formed after the slow addition of 0.21 mol natrium hydroxide (99.98%, Honeywell, Charlotte, NC, USA). The precipitate was centrifuged, and the resulting powder was thermally treated for 7 h at 450 °C.

(ii) $SnO_2$ powder was obtained by dissolving tin tetrachloride ($SnCl_4$, 99.7%, Sigma Aldrich, Munich, Germany) in absolute ethanol (100%, Sigma Aldrich, Munich, Germany). A white solution was obtained after 120 min of stirring at 40 °C. Then, the 0.18 mol of sodium hydroxide (99.98%, Honeywell, Charlotte, NC, USA) was added drop by drop until the gel was formed. The resulting precipitate was centrifuged and the powder was annealed for 5 h at 500 °C.

(iii) $Cu_2S$ powder was obtained from an aqueous solution containing 0.3 mol of copper nitrate ($Cu(NO_3)_2$, 99.9%, Scharlau, Barcelona, Spain) and 0.5 mol of sodium thio-

sulfate ($Na_2S_2O_3$, 99.9%, Scharlau, Barcelona, Spain). The gel was formed after 30 min of stirring and kept in the dark for 6 h to achieve the complete precipitation. After centrifugation, the powder containing intermediary compounds based on $CuS_2O_3$ and $Cu_2S_2O_3$ was thermally treated at 140 °C in a ceramic capsule containing a sulfured (sulfur, 99%, Sigma Aldrich, Munich, Germany) atmosphere. The ceramic capsule was inserted into a furnace (Nabertherm, Lilienthal, Germany) containing an Ar atmosphere (Linde, Dubline, Ireland). The low-oxygen-content atmosphere during the thermal treatment is a pre-requisite to ensure the $Cu_2S$ stoichiometry.

(iv) The $Cu_2S/WO_3$ powder heterostructure was prepared based on the same procedure as described for $Cu_2S$. The $WO_3$ powder was inserted into a copper nitrate precursor considering the Cu:W atomic ratio of 1:1. The sample was annealed at 140 °C for 2 h.

(v) The $Cu_2S/SnO_2$ powder heterostructure was obtained by adding the $SnO_2$ powder into the copper nitrate solution, and the stirring period was increased up to 1 h. The Cu:Sn atomic ratio was 1:1, and the final powder was thermally treated for 3 h at 150 °C.

### 2.2. Photocatalytic Experiments

The photocatalytic activity of the mono-component and the heterostructures was tested into a cylindrical quartz air-proof photoreactor (Sigma Aldrich, Munich, Germany). Firstly, the photoreactor was filled with dry air using a continuous flow rate for 30 min. Secondly, the photoreactor containing 0.05 g of catalyst was injected with 150 ppm acetaldehyde (Linde, Dubline, Ireland). The mixture was kept in the dark for 2 h to reach the absorption equilibrium. Finally, the quartz photoreactor was uniformly irradiated with a UV source (0.08 mW/cm$^2$, 280–400 nm) for 12 h, in order to ensure that photons were evenly distributed on the catalyst surface. The changes in acetaldehyde and carbon dioxide concentrations were recorded by gas chromatography (GC-2014, Shimadzu, Maryland, CO, USA).

### 2.3. Characterization

The formation of the crystalline structure was identified by X-ray diffraction (XRD) analysis made with a Rigaku Miniflex X-Ray diffractometer (Tokyo, Japan) using a Cu $K_\alpha$ source (I = 1.54 Å, 40 kV, 100 mA). The mono-components' and heterostructures' morphology was investigated by field emission scanning electron microscopy (FESEM, SU8010, Fukuoka, Japan) with an accelerated voltage of 25 kV and high-vacuum scanning electron microscopy (SEM, Hitachi model S–3400 N type 121 II, Tokyo, Japan). Both devices were able to investigate the surface elemental composition of the samples. The irradiation source was tested with a class-A high-precision pyranometer (SR11, Hukselflux, Berlin, Germany), and the acetaldehyde degradation was evaluated with gas chromatography (GC-2014, Shimadzu, Maryland, CO, USA).

## 3. Results and Discussions

### 3.1. Composition and Morphology

The diffraction investigations are presented in Figure 1. Table 1 contains the average crystallites size evaluated based on each XRD samples pattern. The results indicate that all mono-component samples contained the crystalline structure corresponding to the designated semiconductor. Monoclinic $WO_3$ (ICCD 83-0951), tetragonal $SnO_2$ (ICCD 41-1445), and orthorhombic $Cu_2S$ (ICCD 20-0365) were formed after the power thermal treatments followed the particular parameters presented in Section 2. The metal oxides presented higher crystallite sizes (93.8 Å for $WO_3$ and 81.5 Å for $SnO_2$) comparatively with $Cu_2S$ (64.7 Å), where milder thermal conditions were used to avoid sulfur sublimation [34–36]. The benchmark samples preserved the stoichiometry of the envisaged compounds that would constitute the basis of heterostructure catalysts and the substrate for $Cu_2S$ development. The heterostructures both contained the crystalline structure of the specific components, but the $Cu_2S$ crystallite size was influenced by the addition of the metal oxide into the synthesis precursor. Consequently, the $Cu_2S$ developed a higher crystallite size in the presence of

$WO_3$, where the space limitation restriction was lower than that of $SnO_2$. These results are similar with other reports [37–39] indicating the $Cu_2S$ will use the highest energy sites, which were, in this case, the metal oxide particle, as preferential nucleation points. The $WO_3$ exhibited the larger crystallite sizes, which favor the $Cu_2S$ growth mechanism and the formation of extensive component interfaces. The $SnO_2$ induced space limitation but had no negative influence on the nucleation process. Even if there were no indications on the formation of other components because of ion diffusion, this process cannot be excluded considering that they may have been in an amorphous state [40–42].
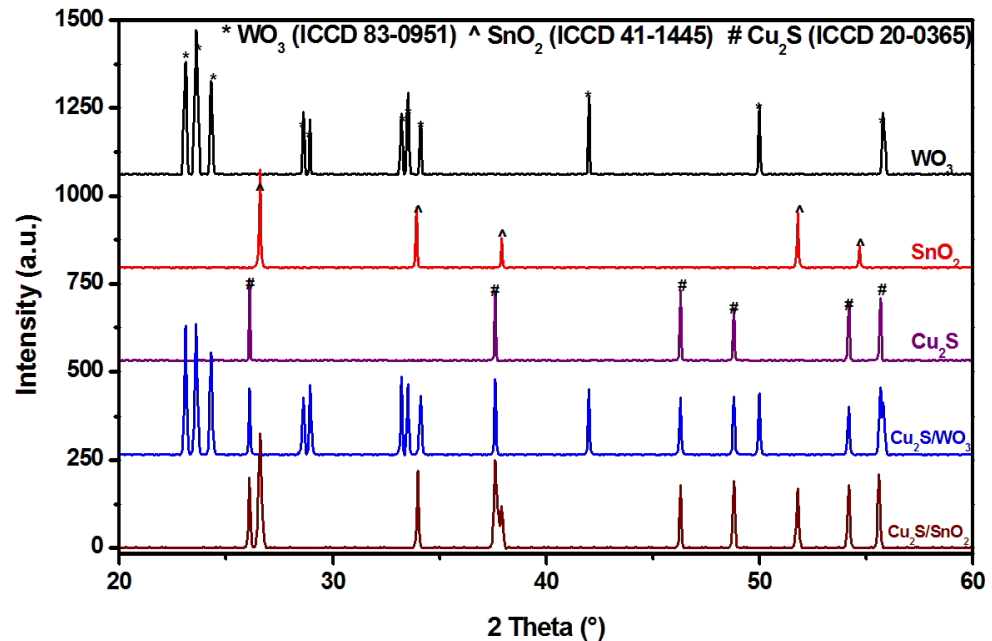


**Figure 1.** X-ray diffraction (XRD) patterns of the mono-component and heterostructure samples.

**Table 1.** Photocatalysts' crystallite size values evaluated based on the Scherrer formula.

| Photocatalyst | Crystallite Size (Å) | | |
|---|---|---|---|
| | $Cu_2S$ | $WO_3$ | $SnO_2$ |
| $WO_3$ | - | 93.8 | - |
| $SnO_2$ | - | - | 81.5 |
| $Cu_2S$ | 64.7 | - | - |
| $Cu_2S/WO_3$ | 82.4 | 92.6 | - |
| $Cu_2S/SnO_2$ | 75.9 | - | 82.6 |

The SEM analysis presented in Figure 2 indicates that the mono-component samples' morphology was severely influenced by the sol-gel synthesis parameters. The metal oxides exhibited dispersed particles, because of the use of an alcoholic precursor, inducing the gel formation during the sodium hydroxide slow addition. The high annealing temperature and NaOH concentration favored the formation of $WO_3$ particles with sizes varying from 0.5 to 2 μm. The use of a lower NaOH concentration and a shorter annealing treatment would induce the formation of small $SnO_2$ particles with an average size of 200 nm. The aqueous precursor employed for $Cu_2S$ synthesis allowed the formation of large aggregates composed of particles with sizes varying from 0.5 to 3 μm. As described by Beneto et al. [43], the heterostructures' morphology is influenced by the insertion of metal oxide particles, which serve as a $Cu_2S$-growing substrate. $Cu_2S/WO_3$ showed a dense morphology containing particles with various shape and sizes combined in a relatively compact assembly. The $Cu_2S$ development was done on small and uniformly distributed $SnO_2$, allowing the formation of a closely connected network with large cavities that can be

used as photoactive sites during the acetaldehyde decomposition [44,45]. The metal oxides had a higher Brunauer-Emmett-Teller (BET) surface area (36.8 m$^2$/g for WO$_3$ and 44.2 m$^2$/g for SnO$_2$) compared with the copper sulfide (21.4 m$^2$/g) component. The heterostructures used the metal oxides as substrates for Cu$_2$S development, which would influence the overall active surface during the photocatalytic activity. Consequently, the Cu$_2$S/SnO$_2$ exhibited a larger BET surface area (41.5 m$^2$/g) than that of Cu$_2$S/WO$_3$ (32.6 m$^2$/g).
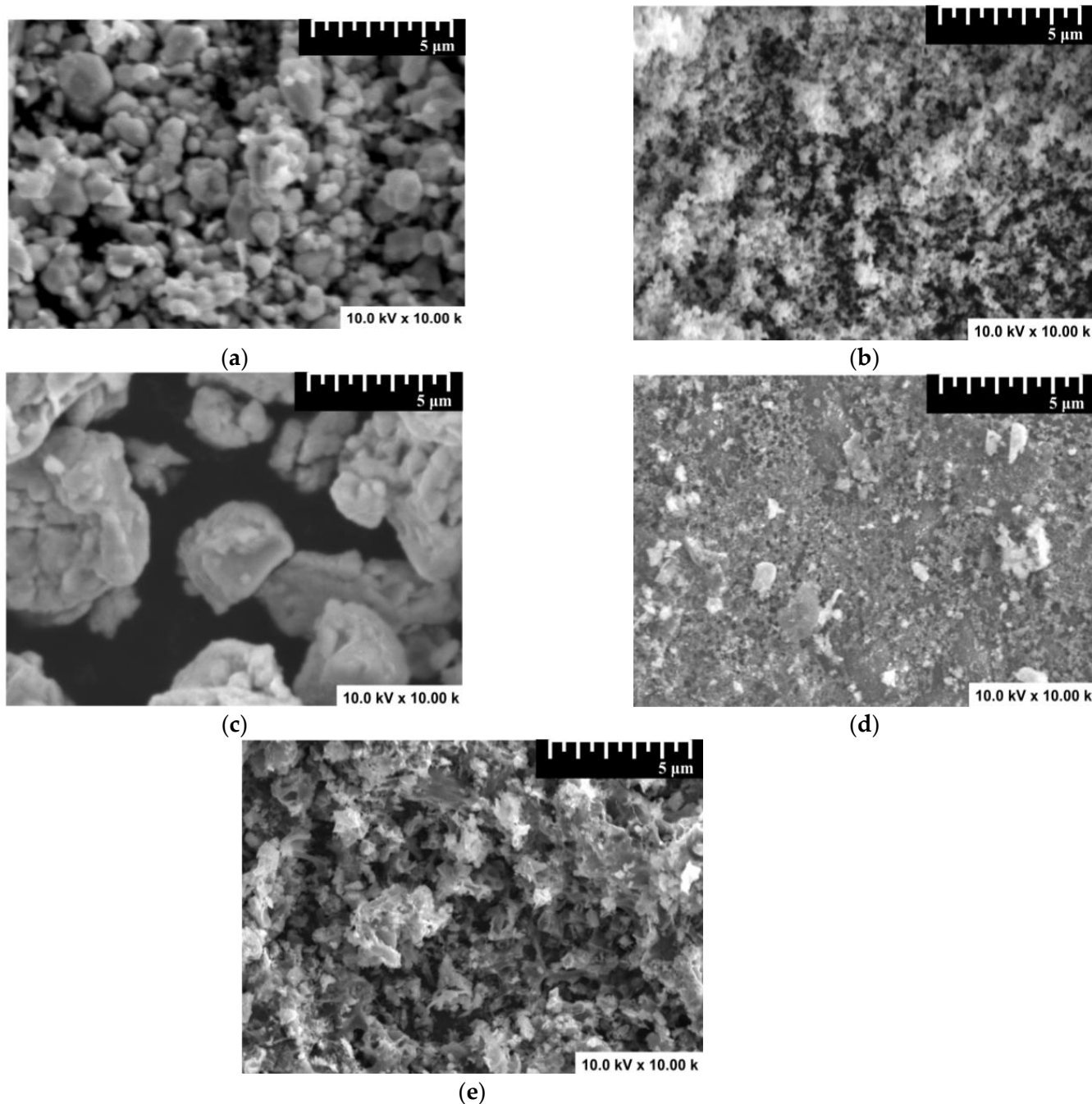


**Figure 2.** Scanning electron microscopy (SEM) images of the photocatalysts: (**a**) WO$_3$, (**b**) SnO$_2$, (**c**) Cu$_2$S, (**d**) Cu$_2$S/WO$_3$, and (**e**) Cu$_2$S/SnO$_2$.

The elemental composition evaluation was done based on energy-dispersive X-ray spectroscopy (EDS) measurements undertaken during the morphology investigations, and the results are presented in Table 2. The investigation was influenced by the bulk composition as the penetration index could not be limited to the surface layer. The sam-

ples' photocatalytic activity depended mostly on the homogenous surface composition, considering that the acetaldehyde removal is an interface-dependent process [46,47]. The results were compared with the theoretical values calculated based on the compounds' stoichiometry identified by the diffraction analysis. The metal oxides' mono-component samples exhibited oxygen excess due to the oxygen atmosphere used for the annealing treatment. However, the $Cu_2S$ benchmark showed a sulfur deficit, which was consistent with other studies [48–50] indicating the tendency of sulfur sublimation during the thermal treatment. The sublimation was significantly reduced by the low thermal temperature treatment and Ar environment around the capsule. Additionally, the presence of a small amount of oxygen in the $Cu_2S$ sample indicates the possible formation of amorphous copper oxide, which was not found by XRD measurements. The heterostructure analysis indicated that the atomic ratio between the metals was preserved as presented in the synthesis method. However, a deficit of oxygen and sulfur was identified in both heterostructure compositions, which was due to the metal oxide's partial coverage with the $Cu_2S$ component. Defect formations, such as vacancies or interstices, were highly expected based on the EDS results and can influence the overall photocatalytic activity.

**Table 2.** Average surface atomic composition of the photocatalysts by energy-dispersive X-ray spectroscopy (EDS).

| Sample | Elemental Composition (% at) | | | | | | |
|---|---|---|---|---|---|---|---|
| | Cu | Sn | W | O | Oth [1] | S | Sth [1] |
| $WO_3$ | - | - | 23.2 | 76.8 | 69.6 | - | - |
| $SnO_2$ | - | 31.4 | - | 68.6 | 62.8 | - | - |
| $Cu_2S$ | 71.5 | - | - | 3.7 | - | 24.8 | 35.7 |
| $Cu_2S/WO_3$ | 17.7 | - | 16.8 | 57.6 | 50.4 | 7.9 | 8.8 |
| $Cu_2S/SnO_2$ | 24.8 | - | 23.1 | 41.3 | 46.2 | 10.8 | 12.4 |

[1] Theoretic content calculated based on the stoichiometry.

### 3.2. Photocatalytic Activity and Mechanism

The photocatalytic activity was performed using a hermetic quartz photoreactor and a catalyst dosage of 0.05 g for 150 ppm acetaldehyde. The acetaldehyde and $CO_2$ concentration evolutions during the experiments were evaluated and are presented in Figure 3a,b. The differences between $CH_3CHO$ removal and $CO_2$ production can be explained by the by-product formations (such as $C_2H_2O_4$, $CH_2O$, etc.), which were not quantified during the experiments. The samples were uniformly irradiated from all sides, using an UV irradiance of 0.08 $mW/cm^2$. The absorption equilibrium was reached after keeping the samples in the dark for 2 h. In the next 12 h, the samples were irradiated and evaluated hourly, in the first 4 h, and at 2 h intervals for the remaining period. Acetaldehyde was considered as a VOC reference because it was found by the International Agency for Research on Cancer to be one of the most frequent indoor air toxins with potential carcinogenic effects [51,52]. The photocatalytic acetaldehyde removal efficiency was calculated considering the initial ($C_0$) and final ($C$) concentrations based on Equation (1):

$$\eta = \left[ \frac{(C_0 - C)}{C_0} \right] \times 100 \tag{1}$$

The mono-component samples exhibited low photocatalytic properties with a maximum 32.3% acetaldehyde removal efficiency for $SnO_2$ and a minimum acetaldehyde removal efficiency of 17.9% for $Cu_2S$. The $WO_3$ sample exhibited a 22% acetaldehyde removal efficiency after 12 h of irradiation and the photocatalytic activity remain stable after 3 cycles. In the same photocatalytic testing condition, $TiO_2$ showed a maximum acetaldehyde removal efficiency of 15% [53], which is similar with bare $Cu_2S$. Another study [54] showed that using composite sheets of titanium dioxide ($TiO_2$) and an adsorbent nylon film with a 0.5–5.0% mass ratio is possible to remove 250 ppm acetaldehyde after

240–300 min irradiation with UV (80 µW/cm$^2$). Titania can be doped with Fe using chemical vapor deposition and thermal treatment at 750 °C [55]. The photocatalytic experiments were done at different relative humidities (0%, 30%, and 60%), and the results indicated that the acetaldehyde removal efficiency was facilitated by the water vapor's content. The complete oxidation of acetaldehyde was gradually enhanced with increasing humidity. Commercial $TiO_2$ was combined with $TaS_2$ to study the photocatalytic degradation of gaseous acetaldehyde [56]. The second component, $TaS_2$, provided two merits: (i) a higher adsorptive capacity of gaseous acetaldehyde compared with $TiO_2$ and (ii) a better separation efficiency of charge carriers. The system was able to remove 98% of acetaldehyde using vis light as an irradiation source.
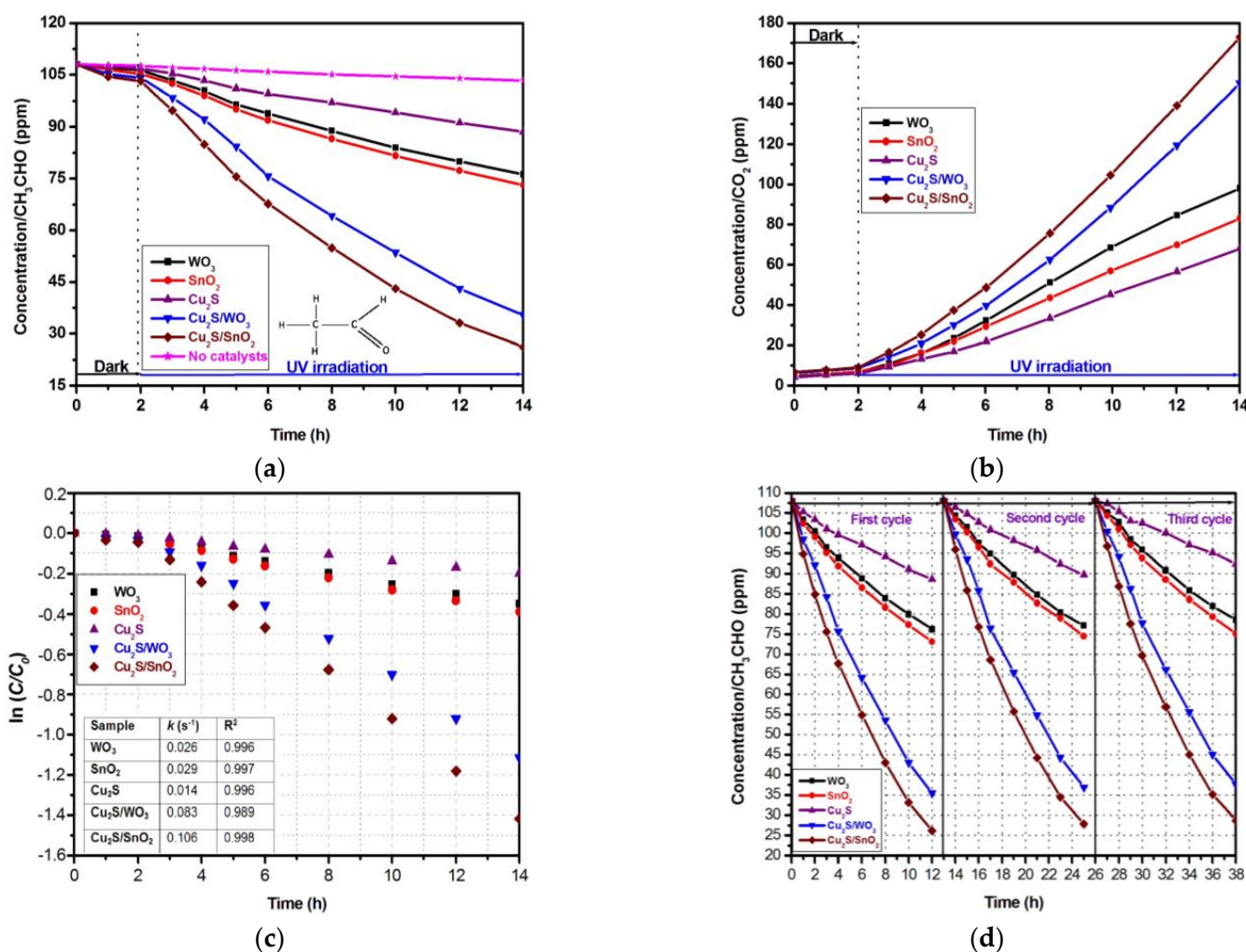


**Figure 3.** Photocatalytic activity of the mono-component and heterostructure samples: (**a**) acetaldehyde removal, (**b**) $CO_2$ formation, (**c**) kinetic evaluation, and (**d**) long stability tests.

The photocatalytic activity increased significantly when heterostructures were involved. The maximum photocatalytic efficiency was obtained for $Cu_2S/SnO_2$ (75.7%), with lamellar morphology allowing cavity formation and a multi-scattering effect. The $Cu_2S/SnO_2$ heterostructure reached 67.2% acetaldehyde removal efficiency, which is consistently higher than that of bare catalysts. The kinetic evaluation presented in Figure 3c was done based on the Langmuir–Hinshelwood model, which considers the concentration, the time (*t*), and the constant rate (*k*) in the following equation:

$$\ln C = \ln C_0 - kt \tag{2}$$

The results indicate a superior constant rate corresponding to the heterostructures' photocatalytic activity, compared with mono-component samples. The $Cu_2S/SnO_2$ exhibited an acetaldehyde degradation rate three times higher than that of $WO_3$ or $SnO_2$ and seven and a half times higher than that of $Cu_2S$. The increase in the photocatalytic performance by developing active heterostructure may be the key for fast VOC removal from indoor spaces. The long-term stability tests presented in Figure 3b indicate small changes of the photocatalytic properties after three cycles, excepting the $Cu_2S$ sample, which showed a significant reduction in the photocatalytic activity between the second and third cycle. However, when coupled with metal oxides in heterostructures, the $Cu_2S$ exhibited good stability as the exposed liquid-catalysts interface was composed of metal oxides and sulfides.

The photocatalytic activity enhancement corresponding to the $Cu_2S/SnO_2$ and $Cu_2S/WO_3$ heterostructures was elucidated by studding the mechanism behind the pollutant mineralization. The production of oxidative species ($HO\cdot$, $\cdot O_2^-$) required charge carriers' transition and migration, which was based on the photon energy conversion during the irradiation. The development of a band energy diagram consisted in evaluating the experimental band-gap values of each component forming the heterostructure and is presented in Figure 4b–d. The methodology is in good agreement with the literature [57,58], considering that the band-gap heterostructures values shift because of the internal energy field. The evaluation of the energy band position, presented in Figure 4a, includes the integration of several parameters such as the free electron energy vs. hydrogen ($E_e$), the absolute cationic electronegativity ($\chi_{cation}$), the semiconductor electronegativity ($\chi_{semiconductor}$), and the specific cationic electronegativity $\chi_{cation}$ (*P.u.*), where *P.u.* represents the Pauling units and band gap energy ($E_g$), into Equations (3)–(6).

$$E_{VB} = \chi_{semiconductor} - E_e + 0.5E_g \tag{3}$$

$$E_{CB} = E_{VB} - E_g \tag{4}$$

$$\chi_{semiconductor}(eV) = 0.45 \times \chi_{cation}(eV) + 3.36 \tag{5}$$

$$\chi_{cation}(eV) = \frac{\chi_{cation}(P.u) + 0.206}{0.336} \tag{6}$$

During the light irradiation, the photogenerated electrons originating from the $Cu_2S$ conduction band ($-0.41$ eV) would be transferred to $SnO_2$ ($+0.54$ eV) or $WO_3$ ($+0.52$ eV) conduction bands. Owing to their potential, the photoinduced electrons from $SnO_2$ and $WO_3$ conduction bands (CB) cannot produce $\cdot O_2^-$, and the photoinduced holes from the $Cu_2S$ valence band ($+0.93$ eV) cannot be involved in $\cdot OH$ generation. These charge carriers cannot be used in the acetaldehyde photocatalytic degradation and will recombine [59–61]. The useful photogenerated electrons from the $Cu_2S$ conduction band ($-0.41$ eV), and the photogenerated holes from $SnO_2$ ($+3.94$ eV)/$WO_3$ ($+3.42$ eV) valence bands, possessed a stronger redox ability. Consequently, these charge carriers can be efficiently separated by the electric field formed in the charged space region. The synergy between the combined drift and diffusion effect would promote the transfer of photogenerated charge carriers through the heterostructure semiconductor components [62–65]. This behavior was attributed to the Z-scheme mechanism able to efficiently convert the photon energy in order to produce the charge carriers involved in the development of (super)oxidative species. The $Cu_2S/SnO_2$ heterostructure benefits from the higher $SnO_2$ conduction band potential required for charge separation and generation of $\cdot OH$ radicals. Additionally, the $Cu_2S/SnO_2$ had a higher BET surface area, which increased the interfacial contact with the pollutant gas where the acetaldehyde decomposition takes place.
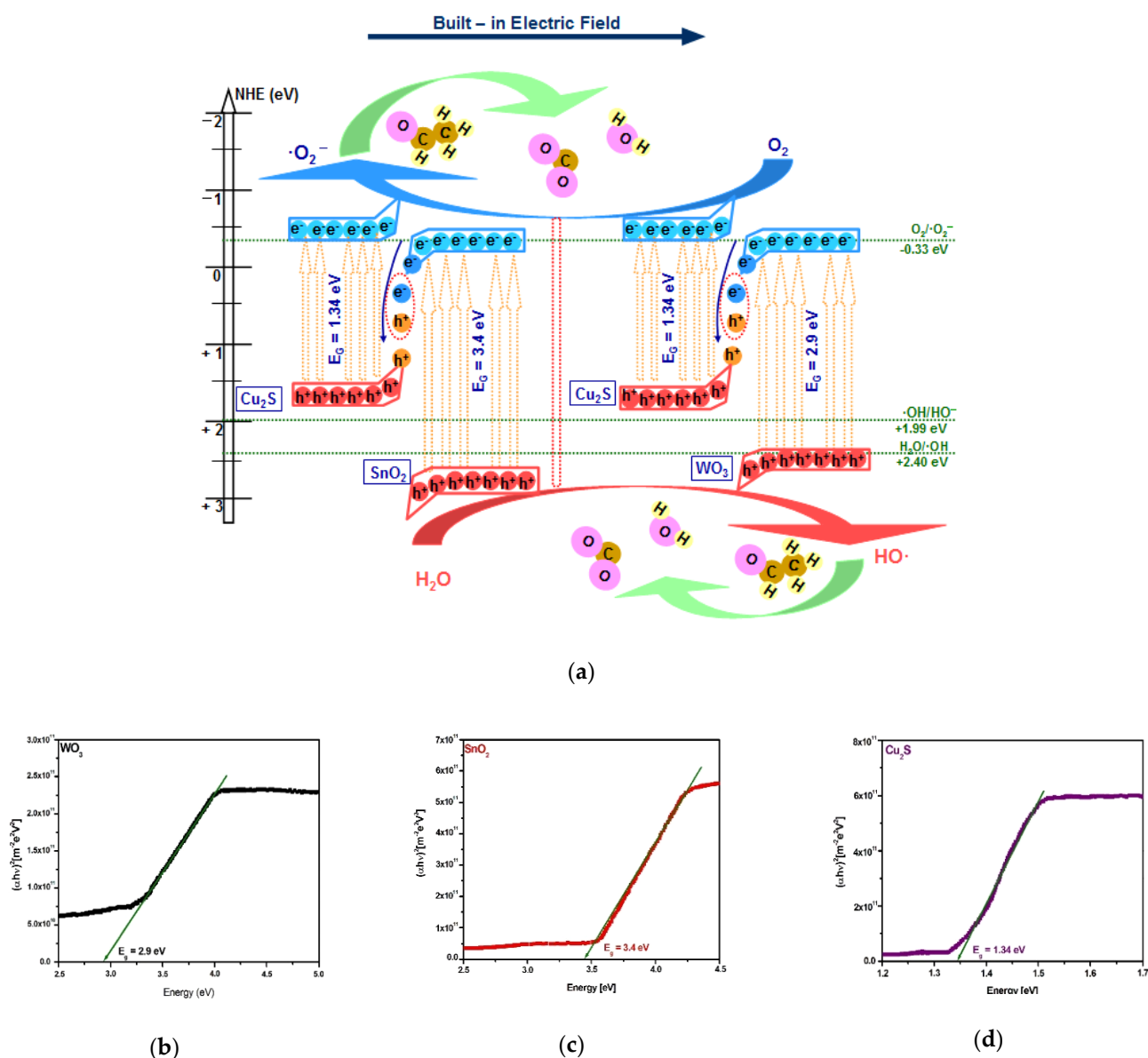
**Figure 4.** (**a**) Heterostructures' Z-scheme mechanism and band-gap values of (**b**) $WO_3$, (**c**) $SnO_2$, and (**d**) $Cu_2S$ semiconductors.

## 4. Conclusions

A simple sol-gel procedure was employed to produce three mono-components ($WO_3$, $SnO_2$, and $Cu_2S$) and two heterostructure ($Cu_2S/WO_3$ and $Cu_2S/SnO_2$) photocatalysts. The metal oxides were used as nucleation sites for $Cu_2S$ development during the synthesis. The samples contained monoclinic $WO_3$, tetragonal $SnO_2$, and orthorhombic $Cu_2S$ crystalline structures. The $Cu_2S$ crystallite size in the heterostructures varied from 75.9 to 82.4 Å, depending on the metal oxide substrate. The $Cu_2S/WO_3$ morphology was characterized by a compact assembly of particles with various sizes and shapes. The surface elemental composition indicated that both heterostructures exhibited an oxygen and sulfur deficit, compared with the stoichiometric composition.

The photocatalytic removal of acetaldehyde was done using a 0.08 mW/cm$^2$ UV irradiance. The heterostructures had a significantly higher photocatalytic activity compared with the bare samples. The $Cu_2S/SnO_2$ and $Cu_2S/WO_3$ followed a Z-scheme mechanism allowing the efficient use of charge carriers with a stronger redox ability. The highest photocatalytic efficiency (75.7%) corresponded to $Cu_2S/SnO_2$, with a constant rate of 0.106 s$^{-1}$ (which was three times faster than $WO_3$ or $SnO_2$ and seven and a half times faster

than Cu$_2$S). The use of the Z-scheme-mechanism heterostructures can improve the photon energy conversion and reduce the useful charge carrier recombination. The results indicate that the heterostructures containing Cu$_2$S have a better stability of the photocatalytic activity compared with the bare Cu$_2$S. The main issues were represented by the necessity to increase the photocatalytic efficiency in the presence of a wider light spectrum (UV and vis). Future work will investigate the optimization of heterostructure composition for sunlight applications.

**Author Contributions:** Conceptualization, A.E.; methodology, A.E.; software, L.I.; validation, A.E. and L.I.; formal analysis, L.I.; investigation, L.I.; resources, A.E.; data curation, L.I.; writing—original draft preparation, A.E.; writing—review and editing, A.E.; visualization, L.I.; supervision, A.E.; project administration, A.E.; funding acquisition, A.E. All authors have read and agreed to the published version of the manuscript.

**Institutional Review Board Statement:** Not applicable.

**Informed Consent Statement:** Not applicable.

**Data Availability Statement:** Data presented in this study are available by requesting from the corresponding author.

**Conflicts of Interest:** The authors declare no conflict of interest.

# References

1. Xiang, W.; Han, X.; Astorsdotter, J.; Farrauto, R. Catalysts Promoted with Niobium Oxide for Air Pollution Abatement. *Catalysts* **2017**, *7*, 144. [CrossRef]
2. Xu, R.; Alam, M.S.; Harrison, R.M. Behaviour of traffic emitted semi-volatile and intermediate volatility organic compounds within the urban atmosphere. *Sci. Total Environ.* **2020**, *720*, 137470. [CrossRef] [PubMed]
3. Sanito, R.C.; You, S.J.; Wang, Y.F. Effect of shell powder on removal of metals and volatile organic compounds (VOCs) from resin in an atmospheric-pressure microwave plasma reactor. *J. Hazard. Mater.* **2020**, *394*, 122558. [CrossRef] [PubMed]
4. Wang, H.; Wang, Y.; Hou, X.; Xiong, B. Bioelectronic Nose Based on Single-Stranded DNA and Single-Walled Carbon Nanotube to Identify a Major Plant Volatile Organic Compound (p-Ethylphenol) Released by Phytophthora Cactorum Infected Strawberries. *Nanomaterials* **2020**, *10*, 479. [CrossRef]
5. He, W.; Shi, A.; Li, G. Insights into the comprehensive characteristics of volatile organic compounds from multiple cooking emissions and aftertreatment control technologies application. *Atmos. Environ.* **2020**, *240*, 117646. [CrossRef]
6. Qiu, Y.; Ye, N.; Situ, D.; Zuo, S.; Wang, X. Study of Catalytic Combustion of Chlorobenzene and Temperature Programmed Reactions over CrCeOx/AlFe Pillared Clay Catalysts. *Materials* **2019**, *12*, 728. [CrossRef]
7. Abdelkader, E.; Nadjia, L.; Noureddine, B. SnO$_2$ foam grain-shaped nanoparticles: Synthesis, characterization and UVA light induced photocatalysis. *J. Alloy. Compound.* **2016**, *679*, 408–419. [CrossRef]
8. He, J.; Zou, Z.; Yang, X. Measuring whole-body volatile organic compound emission by humans: A pilot study using an air-tight environmental chamber. *Build. Environ.* **2019**, *153*, 101–109. [CrossRef]
9. Zhao, Q.; Li, Y.; Tian, S. Interaction of inhalable volatile organic compounds and pulmonary surfactant: Potential hazards of VOCs exposure to lung. *J. Hazard. Mater.* **2019**, *369*, 512–520. [CrossRef]
10. Noh, H.L.; Park, Y.K.; Kim, J.H. Colorimetric chemosensor for detection of a volatile organic compound, ethylamine, under versatile conditions: Solution, thin-film, and dyed fabric. *Sens. Actuat. B* **2019**, *301*, 127079. [CrossRef]
11. Dong, N.; Ye, Q.; Chen, M.; Cheng, S.; Kang, T.; Dai, H. Catalytic Oxidation of HCHO over the Sodium-Treated Sepiolite-Supported Rare Earth (La, Eu, Dy, and Tm) Oxide Catalysts. *Catalysts* **2020**, *10*, 328. [CrossRef]
12. Ojha, D.P.; Song, J.H.; Kim, H.J. Facile synthesis of graphitic carbon-nitride supported antimony-doped tin oxide nanocomposite and its application for the adsorption of volatile organic compounds. *J. Environ. Sci.* **2019**, *79*, 35–42. [CrossRef] [PubMed]
13. Zare, F.D.; Allahdadlalouni, M.; Bagheri, H. Reduced graphene oxide–melamine formaldehyde as a highly efficient platform for needle trap microextraction of volatile organic compounds. *Microchem. J.* **2020**, *157*, 104932. [CrossRef]
14. Asencios, Y.J.O.; Quijo, M.V.; Assaf, E.M. Photocatalytic activity of Nb heterostructure (NaNbO$_3$/Na$_2$Nb$_4$O$_{11}$) and Nb/clay materials in the degradation of organic compounds. *Sol. Energy* **2019**, *194*, 37–46. [CrossRef]
15. Enesca, A.; Isac, L.; Duta, A. Charge carriers injection in tandem semiconductors for dyes mineralization. *Appl. Catal. B.* **2015**, *162*, 352–363. [CrossRef]

16. Liu, B.; Long, M.; Yang, J. Interfacial charge behavior modulation in 2D/3D perovskite heterostructure for potential high-performance solar cells. *Nano Energy* **2019**, *59*, 715–720. [CrossRef]

17. Anaya-Esparza, L.M.; Montalvo-González, E.; González-Silva, N.; Méndez-Robles, M.D.; Romero-Toledo, R.; Yahia, E.M.; Pérez-Larios, A. Synthesis and Characterization of $TiO_2$-ZnO-MgO Mixed Oxide and Their Antibacterial Activity. *Materials* **2019**, *12*, 698. [CrossRef]

18. Spanu, D.; Recchia, S.; Altomare, M. Site-selective Pt dewetting on $WO_3$-coated $TiO_2$ nanotube arrays: An electron transfer cascade-based $H_2$ evolution photocatalyst. *Appl. Catal. B* **2018**, *237*, 198–205. [CrossRef]

19. Singhal, S.; Dixit, S.; Shukla, A.K. Self-assembly of the Ag deposited ZnO/carbon nanospheres: A resourceful photocatalyst for efficient photocatalytic degradation of methylene blue dye in water. *Adv. Powder Technol.* **2018**, *29*, 3483–3492. [CrossRef]

20. Li, X.; Peng, T.; Nan, Z. A new efficient visible-light photocatalyst made of $SnO_2$ and cyclized polyacrylonitrile. *Mater. Res. Bull.* **2018**, *97*, 517–522. [CrossRef]

21. Do, J.Y.; Chava, R.K.; Kang, M. Fabrication of core@interface:shell structured $CuS@CuInS_2$:$In_2S_3$ particles for highly efficient solar hydrogen production. *Appl. Surf. Sci.* **2018**, *451*, 86–98. [CrossRef]

22. Das, D.; Nandi, P. Ternary ZnCdSO composite photocatalyst for efficient dye degradation under visible light retaining Z-scheme of migration pathways for the photogenerated charge carriers. *Sol. Energ. Mat. Sol. C.* **2020**, *217*, 110674. [CrossRef]

23. Yusuff, A.S.; Popoola, L.T.; Aderibigbe, E.I. Solar photocatalytic degradation of organic pollutants in textile industry wastewater by ZnO/pumice composite photocatalyst. *J. Environ. Chem. Eng.* **2020**, *8*, 103907. [CrossRef]

24. Kuang, M.; Zhang, J.; Ji, Z. The effect of support on the structure and photocatalytic activity of ternary $ZnO$-$ZnFe_2O_4$/palygorskite composite photocatalysts. *Adv. Powder Technol.* **2020**, *31*, 1–10. [CrossRef]

25. Peng, Z.Y.; Jiang, Y.; Ni, L. Novel CdIn2S4 nano-octahedra/$TiO_2$ hollow hybrid heterostructure: In-situ synthesis, synergistic effect and enhanced dual-functional photocatalytic activities. *Ceram. Int.* **2019**, *45*, 15942–15953. [CrossRef]

26. Matsunami, D.; Yamanaka, K.; Kojima, K. Comparison of photodegradation of methylene blue using various $TiO_2$ films and $WO_3$ powders under ultraviolet and visible-light irradiation. *J. Photochem. Photobiol. A* **2019**, *369*, 106–114. [CrossRef]

27. Chen, S.; Liu, F.; Liu, C. First-principles calculations and experimental investigation on $SnO_2@ZnO$ heterojunction photocatalyst with enhanced photocatalytic performance. *J. Colloid Interfac. Sci.* **2019**, *553*, 613–621. [CrossRef]

28. Meroni, D.; Gasparini, C.; Bianchi, C.L. Ultrasound-assisted synthesis of ZnO photocatalysts for gas phase pollutant remediation: Role of the synthetic parameters and of promotion with $WO_3$. *Ultrason. Sonochem.* **2020**, *66*, 105119. [CrossRef]

29. Bravo, I.; Figueroa, F.; Swasy, M.I.; Attia, M.F.; Ateia, M.; Encalada, D.; Vizuete, K.; Galeas, S.; Guerrero, V.H.; Debut, A.; et al. Cellulose particles capture aldehyde VOC pollutants. *RSC Adv.* **2020**, *10*, 7967–7975. [CrossRef]

30. Kumar, V.; Lee, Y.S.; Shin, J.W.; Kim, K.H.; Kukkar, D.; Fai Tsang, Y. Potential applications of graphene-based nanomaterials as adsorbent for removal of volatile organic compounds. *Environ. Int.* **2020**, *135*, 105356. [CrossRef]

31. Demeestere, K.; Dewulf, J.; De Witte, B.; Beeldens, A.; Van Langenhove, H. Heterogeneous photocatalytic removal of toluene from air on building materials enriched with $TiO_2$. *Build. Environ.* **2008**, *43*, 406–414. [CrossRef]

32. Seo, H.O.; Park, E.J.; Kim, I.H.; Han, S.W.; Cha, B.J.; Woo, T.G.; Kim, Y.D. Influence of humidity on the photo-catalytic degradation of acetaldehyde over $TiO_2$ surface under UV light irradiation. *Catal. Today* **2017**, *295*, 102–109. [CrossRef]

33. Jeong, M.G.; Park, E.J.; Seo, H.O.; Kim, K.D.; Kim, Y.D.; Lim, D.C. Humidity effect on photocatalytic activity of $TiO_2$ and regeneration of deactivated photocatalysts. *Appl. Surf. Sci.* **2013**, *271*, 164–170. [CrossRef]

34. Chaugule, A.A.; Pawar, A.A.; Kim, H. Ionic liquid based $Cu_2S@C$ catalyst for effective coupling of diaryl diselenide with aryl halides under ligand-free conditions. *Chem. Eng. J.* **2018**, *351*, 490–497. [CrossRef]

35. Zhang, J.; Li, W.; Xu, C. Self-optimizing bifunctional $CdS/Cu_2S$ with coexistence of light-reduced $Cu^0$ for highly efficient photocatalytic $H_2$ generation under visible-light irradiation. *Appl. Catal. B* **2017**, *217*, 30–36. [CrossRef]

36. Gao, H.; Zhai, C.; Zhu, M. Snowflake-like $Cu_2S$ as visible-light-carrier for boosting Pd electrocatalytic ethylene glycol oxidation under visible light irradiation. *Electrochim. Acta* **2020**, *330*, 135214. [CrossRef]

37. Iqbal, S.; Bahadur, A.; Shoaib, M. Shape and phase-controlled synthesis of specially designed 2D morphologies of l-cysteine surface capped covellite (CuS) and chalcocite ($Cu_2S$) with excellent photocatalytic properties in the visible spectrum. *Appl. Surf. Sci.* **2020**, *526*, 146691. [CrossRef]

38. Li, L.; Zhang, W.; Chen, W. $Cu_2S$/CIGS core/shell nanowire arrays with epitaxial CIGS growth. *Sol. Energ. Mater. Sol. C.* **2014**, *128*, 357–361. [CrossRef]

39. Fu, Y.; Jin, W. Facile synthesis of core-shell $CuS$-$Cu_2S$ based nanocomposite for the high-performance glucose detection. *Mater. Sci. Eng. C* **2019**, *105*, 110120. [CrossRef]

40. Ghifari, A.; Long, D.X.; Kim, S.; Ma, B.; Hong, J. Transparent Platinum Counter Electrode Prepared by Polyol Reduction for Bifacial, Dye-Sensitized Solar Cells. *Nanomaterials* **2020**, *10*, 502. [CrossRef]

41. Dudita, M.; Bogatu, C.; Enesca, A.; Duta, A. The influence of the additives composition and concentration on the properties of $SnO_x$ thin films used in photocatalysis. *Mater. Lett.* **2011**, *65*, 2185–2189. [CrossRef]

42. Bagherian, S.; Zak, A.K. X-ray peak broadening and optical properties analysis of $SnO_2$ nanosheets prepared by sol-gel method. *Mater. Sci. Semicon. Proc.* **2016**, *56*, 52–58. [CrossRef]

43. Baneto, M.; Enesca, A.; Mihoreanu, C.; Lare, Y.; Jondo, K.; Napo, K.; Duta, A. Effects of the growth temperature on the properties of spray deposited $CuInS_2$ thin films for photovoltaic applications. *Ceram. Int.* **2015**, *41*, 4742–4749. [CrossRef]

44. Liu, Y.; Ye, Z.; Huang, W. Tuning $CuO_x$-$TiO_2$ interaction and photocatalytic hydrogen production of $CuO_x$/$TiO_2$ photocatalysts via $TiO_2$ morphology engineering. *Appl. Surf. Sci.* **2019**, *473*, 500–510. [CrossRef]

45. Lei, E.; Hu, C.; Liu, Z. Composition, morphology, structure and photocatalytic performances of photocatalysts prepared from titanium potassium oxalate. *Solid State Sci.* **2019**, *88*, 36–40. [CrossRef]

46. Liang, Q.; Liu, X.; Gong, S. Surfactant-assisted synthesis of photocatalysts: Mechanism, synthesis, recent advances and environmental application. *Chem. Eng. J.* **2019**, *372*, 429–451. [CrossRef]

47. Li, L.; Yan, Y.; Zhou, J. Glucose-assisted hydrothermal synthesis of plasmonic Bi deposited nested $Bi_2O_2-xCO_3$ photocatalysts with enhanced photocatalytic activity. *Colloid. Surf. A* **2019**, *583*, 123946. [CrossRef]

48. Tang, Q.Y.; Chen, W.F.; Lv, Y.R.; Yang, S.Y.; Xu, Y.H. Z-scheme hierarchical $Cu_2S$/$Bi_2WO_6$ composites for improved photocatalytic activity of glyphosate degradation under visible light irradiation. *Sep. Purif. Technol.* **2020**, *236*, 116243. [CrossRef]

49. Sithole, R.K.; Machogo, L.F.E.; Moloto, N. One-step synthesis of $Cu_3N$, $Cu_2S$ and $Cu_9S_5$ and photocatalytic degradation of methyl orange and methylene blue. *J. Photochem. Photobiol. A* **2020**, *397*, 112577. [CrossRef]

50. Jo, I.R.; Rajesh, J.A.; Ahn, K.S. Enhanced electrocatalytic activity and electrochemical stability of $Cu_2S$/PbS counter electrode for quantum-dot-sensitized solar cells. *Appl. Surf. Sci.* **2020**, *525*, 146643. [CrossRef]

51. Serinçay, N.; Fellah, M.F. Acetaldehyde adsorption and detection: A density functional theory study on Al-doped graphene. *Vacuum* **2020**, *175*, 109279. [CrossRef]

52. Zeng, Q.; Wang, X.; Sun, J. Band bending of $TiO_2$ induced by O-xylene and acetaldehyde adsorption and its effect on the generation of active radicals. *J. Colloid Interface Sci.* **2020**, *572*, 374–383. [CrossRef]

53. Enesca, A. Enhancing the Photocatalytic Activity of $SnO_2$-$TiO_2$ and ZnO-$TiO_2$ Tandem Structures Toward Indoor Air Decontamination. *Front. Chem.* **2020**, *8*, 583270. [CrossRef] [PubMed]

54. Ichiura, H.; Seike, T.; Kozu, A. Acetaldehyde gas removal by a nylon film–$TiO_2$ composite sheet prepared on a paper surface using interfacial polymerization and electrostatic interactions. *Chemosphere* **2020**, *256*, 127143. [CrossRef] [PubMed]

55. Saqlain, S.; Cha, B.J.; Kim, S.Y.; Sung, J.Y.; Choi, M.C.; Seo, H.O.; Kim, Y.D. Impact of humidity on the removal of volatile organic compounds over Fe loaded $TiO_2$ under visible light irradiation: Insight into photocatalysis mechanism by operando DRIFTS. *Mater. Today Commun.* **2021**, *26*, 102119. [CrossRef]

56. Zeng, Q.; Wang, X.; Xie, X.; Lu, G.; Wang, Y.; Lee, S.C.; Sun, J. $TiO_2$/$TaS_2$ with superior charge separation and adsorptive capacity to the photodegradation of gaseous acetaldehyde. *Chem. Eng. J.* **2020**, *379*, 122395. [CrossRef]

57. Gao, C.; Li, J.; Shan, Z.; Huang, F.; Shen, H. Preparation and visible-light photocatalytic activity of $In_2S_3$/$TiO_2$ composite. *Mater. Chem. Phys.* **2010**, *122*, 183–187. [CrossRef]

58. Mise, T.; Nakada, T. Low temperature growth and properties of Cu–In–Te based 433 thin films for narrow bandgap solar cells. *Thin Solid Films* **2010**, *518*, 5604–5609. [CrossRef]

59. Iqbal, M.; Wang, Y.; He, T. Interfacial charge kinetics of ZnO/ZnTe heterostructured nanorod arrays for $CO_2$ photoreduction. *Electrochim. Acta* **2018**, *272*, 203–211. [CrossRef]

60. Mouchaal, Y.; Enesca, A.; Mihoreanu, C.; Khelil, A.; Duta, A. Tuning the opto-electrical properties of $SnO_2$ thin films by Ag+1 and In+3 co-doping. *Mater. Sci. Eng. B Adv.* **2015**, *199*, 22–29. [CrossRef]

61. Xiang, Y.; Yu, N.; Cao, L. Simple fabrication of ZnO nanosheets/p-GaN heterostructure and ultraviolet detection. *Physica E* **2018**, *102*, 29–32. [CrossRef]

62. Tian, W.; Wu, H.; Yang, X. Heterostructure based on silver/silver chloride nanocubes loaded titanium dioxide nanofibers: A high-efficient and recyclable visible light-responsive photocatalyst. *J. Photochem. Photobiol. A* **2018**, *350*, 122–129. [CrossRef]

63. Mu, C.; Song, J.; Xiang, J. Facile-synthesized carbonaceous photonic crystals/magnetic particle nanohybrids with heterostructure as an excellent microwave absorber. *J. Alloy. Compound.* **2018**, *741*, 814–820. [CrossRef]

64. Chen, Y.; Li, H.; Yang, P. ZIF-8 derived hexagonal-like $\alpha$-$Fe_2O_3$/ZnO/Au nanoplates with tunable surface heterostructures for superior ethanol gas-sensing performance. *Appl. Surf. Sci.* **2018**, *439*, 649–659. [CrossRef]

65. Liu, J.; Liu, R.; Kuikka, S. Quantifying and predicting ecological and human health risks for binary heavy metal pollution accidents at the watershed scale using Bayesian Networks. *Environ. Pollut.* **2021**, *269*, 116125. [CrossRef]